Technical Paper

The effect of spindle dynamics on tool-tip radial throw in micromachining

Shivang Shekhar[a,1], Sudhanshu Nahata[a,b,1], O. Burak Ozdoganlar[a,c,d,*]

[a] Department of Mechanical Engineering, Carnegie Mellon University, Pittsburgh, PA 15213, USA
[b] ASML US, Wilton, CT 06897, USA
[c] Department of Material Science and Engineering, Carnegie Mellon University, Pittsburgh, PA 15213, USA
[d] Department of Biomedical Engineering, Carnegie Mellon University, Pittsburgh, PA 15213, USA

ABSTRACT

In this work, we present a model to predict the speed-dependent radial throw at the tool-tip during micromachining with ultra-high-speed (UHS) spindles. This speed-dependent nature of the radial throw arises from the interaction between the quasi-static radial throw (tool attachment errors, tool geometric errors, and spindle error motions) and the dynamic response of the tool-collet-spindle system. The radial throw causes the cutting edge trajectory to deviate from the ideal trajectory, critically affecting the attainable dimensional accuracy and surface quality, as well as the micromachining forces. Hence, accurate determination of radial throw at the micro-tool tip is important for both practical applications and process-modeling efforts. In the current work, the proposed model describes the radial throw of the tool-axis as a dynamic response to excitation from rotating unbalance of the spindle assembly. The model parameters are first calibrated using experimentally obtained spindle dynamics and the radial throw measurements, both at two speeds. The calibrated model is then used to predict the radial throw for any spindle speed. The presented model is used to predict radial throw at two different axial locations (microtool's shaft at 2 mm and its tool-tip at 15 mm). For both the axial locations, the spindle dynamics measured at 2 mm is used for model calibration. The average error is observed to be less than 2.4% at the tool-tip (15 mm). It is concluded that the speed-dependent spindle dynamics can be used in an analytical formulation to determine tool-tip radial throw at any speed.

1. Introduction

Micro-scale material removal processes such as micro-milling or micro-drilling, are capable to machine three-dimensional geometries in a variety of materials, including metals, polymers and composites [1–7]. These processes are widely used to make intricate features for a range of applications [1,4–7]. Micromachining processes use ultra-high-speeds (UHS) spindles (> 60,000 revolutions per minute) with micro-scale tools (as small as 20 μm in diameter). One of the prevailing issues with micromachining processes is the deviation in the trajectory of cutting edges from their ideal trajectory. These deviations directly impact the dimensional accuracy and surface finish of the machined components [8–11]. Additionally, the accurate determination of cutting edge trajectory is required for using force models [12–14] and for obtaining micromachining stability lobe diagrams [15–17]. The non-ideal deviations of cutting edge trajectories can be calculated by experimental determination of radial throw of the tool-axis at the tool-tip [10,18,19]. However, when the tool is rotated at a different speed, the

radial throw changes requiring a new set of measurements. Hence, it is important to relate the radial throw with the physical properties of the system, furthermore understanding on eliminating the need for extensive measurements.

Radial throw of tool-axis is a vector defined by a magnitude and an orientation [10,18]. The magnitude defines the radial offset between the tool-axis and the average axis of rotation, in a plane perpendicular to the average axis of rotation [18]. The orientation is defined with respect to a cutting-edge of the tool (or any other fixed reference on the tool). The orientation is the angular location of the radial offset measured from the cutting-edge of the tool in a plane perpendicular to the average axis of rotation. Together, the magnitude and orientation of radial throw are used to calculate the physical location of the cutting edges and hence its trajectory while the tool is rotating [10,19].

Radial throw arises from the kinematics and the speed-dependent dynamics of the tool-collet-spindle assembly [10,18,20,21]. Therefore, radial throw can be classified into two components: quasi-static and dynamic. The quasi-static component of radial throw arises from the

Nomenclature		z_i	*ith* axial location
		θ	angular distance from *x*-axis
m_e	effective unbalance mass	e	eccentricity
ρ_{0d}	location of unbalance mass	ζ	tilt
ρ_0	radial throw, static	δ	change in orientation of radial throw from $z = 0$ and
ρ_d	radial throw, dynamic		$z = z_{-t}$
ρ	radial throw, includes both static and dynamic portions	F_e	force arising from rotating unbalance
η	orientation of radial throw w.r.t. cutting edge of the tool		

geometric inaccuracies of the tool-collet-spindle assembly and their interfaces. The dynamic component of radial throw arises from the speed-dependent dynamics of the tool-collet-spindle assembly as a response to a rotating unbalance excitation [18,20–22]. As a result, the magnitude and orientation of radial throw change with the rotation angle, resulting in a non-trivial 2D trajectory. Radial throw, unlike *run-out*, is capable of describing the true trajectory of the tool-axis perpendicular of the average axis of rotation.

A majority of research in the literature focuses on run-out measurement (ignoring the 2D nature) [23–28], measurement of radial throw [10,19,29,30] at specific speeds or estimating run-out from cutting force measurements [24,25,28] or from feed marks [26]. As measurement at the tool-tip is difficult due to the presence of flutes, eccentricity and tilts are calculated from the measurements at the tool-shank which are then used to predict at the tool-tip [10,19,27]. New measurements are needed each time a new speed is selected. As a result, the determination of radial throw at the tool-tip becomes time consuming, costly and impacts the yield. Therefore, methods are needed to predict the tool-tip radial throw while minimizing the need for measurements to meet the industrial demands.

A direct correlation has been observed between radial throw magnitude and displacement-to-force frequency response functions [20,21]. Since the dynamic part of radial throw results from rotating unbalance excitation, an estimate of unbalance eccentricity is required for radial throw predictions. In [31], it was shown that unbalance parameters for a macro-scale rotor can be determined from a single run-down or run-up of the machine, when *a priori* rotor and bearing model is available. Such models do not exist at the micro-scale for UHS spindles and experimental characterization of dynamics is the only reliable option. Therefore, dynamic characterization of tool-collet-spindle assembly is essential [21]. However, there is still a gap in literature regarding quantitative prediction of radial throw using the dynamics of UHS spindles.

As discussed earlier, the 2D trajectory of radial throw is non-trivial and contains offsets originating from geometric inaccuracies of the components/assembly and radial motions from rotating unbalance type excitation. As a result, the trajectory of radial throw is considerably complex and contains many harmonics [30]. However, the synchronous (one-per-rev) component of radial throw that includes the tool-attachment errors, shaft/bearing misalignment and dynamic response from the rotating unbalance has the largest ($> 90\%$) contribution to the overall magnitude [30,32]. Therefore, for this study, we focus on the prediction of synchronous component of radial throw of tool-axis, the general trajectory of which can be described as an ellipse about the average axis of rotation. We present an analytical framework to predict the speed-dependent radial throw at the tool-tip for UHS micro-machining spindles. The framework utilizes an analytical-based dynamic unbalance response model. The model uses speed-dependent dynamics and a set of radial throw measurements. A curve-fitting based calibration approach is used to obtain the parameters of the model. Using the obtained model parameters and the spindle dynamics, the developed model can predict radial throw at any given spindle speed. To this end, we perform spindle dynamics characterization at five different speeds. Next, we use radial throw measurements at two spindle speeds to obtain the model parameters. We then use the model to
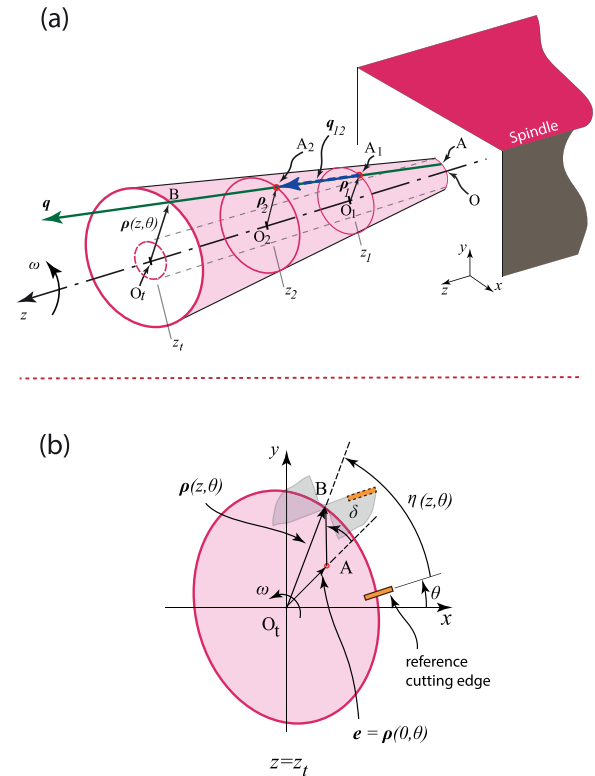

Fig. 1. Accurate determination of radial throw: (a) The tool-axis **q** and its relationship with the rotational axis Ot, and (b) the planar view of the tool tip and the description of radial throw parameters in $x - y$ plane at the tool tip.

predict radial throw at the remaining speeds and validate them with the actual measurements.

2. Modeling

Fig. 1 describes the radial throw of tool-axis O_1A_1, O_2A_2 and O_tB at axial planes z_1, z_2 and z_t, respectively. The tool-axis is defined by a vector **q**, with its origin at the spindle nose. The tool is rotated about an average axis of rotation passing through OO_t, and θ is the rotation angle of the tool measured counterclockwise from the *x*-axis. Radial throw is described by a magnitude $\rho(z, \theta)$ and an orientation $\eta(z, \theta)$, both of which are dependent on the axial location and the rotation angle of the tool. The deviation of tool-axis from the average axis of rotation is defined by an eccentricity $e = e(\theta)$ and a tilt $\zeta = \zeta(\theta)$. The average magnitude of radial throw typically increases with axial distance from spindle nose because of increasing contribution from tilts. Because of the three-dimensional nature of tilts, the orientation of radial throw also varies with axial distance (e.g., notice the change in the orientation of vectors OA (at $z = 0$) and OB ($z = z_t$) in Fig. 1(b)) and this variation in radial throw orientation is defined by δ.

The physical measurements of radial throw at the tool-tip is difficult due to the presence of flutes. Therefore, accurate determination of radial throw at the tool-tip is enabled by measurements at any two axial

locations on the tool-shank. These measurements provide x and y components of ρ at the two axial locations, i.e.,

$$\boldsymbol{\rho_1} = \boldsymbol{\rho}(z_1, \theta) = \rho_{1x}\boldsymbol{i} + \rho_{1y}\boldsymbol{j}, \tag{1}$$

$$\boldsymbol{\rho_2} = \boldsymbol{\rho}(z_2, \theta) = \rho_{2x}\boldsymbol{i} + \rho_{2y}\boldsymbol{j}. \tag{2}$$

where $\boldsymbol{i}$ and $\boldsymbol{j}$ are the unit vectors along the x and y directions, respectively. Using a vector-based approach [10], vector $\mathbf{q}_{12}$ along the tool-axis is determined. This vector is used to calculate the eccentricity e and tilt ζ of the tool-axis. Once known, e and ζ can be used to calculated radial throw at any axial location [10]. This method is used to calculate radial throw at the tool-tip for two spindle speeds, which serves as an input to the model for estimating unbalance parameters.

Fig. 2 represents the physical model used to describe the rotating unbalance type excitation in the $x - y$ plane located at $z = z_t$. The equivalent stiffness along the x and y directions are generally different (axi-asymmetric). The force arising from the rotating unbalance effect can be expressed as

$$\boldsymbol{F_e} = \begin{Bmatrix} F_{ex} \\ F_{ey} \end{Bmatrix} = m_e \rho_{0d}\omega^2 \begin{Bmatrix} 1 \\ -j \end{Bmatrix} e^{j\omega t}, \tag{3}$$

where ω is the rotational frequency, m_e is the *effective* unbalance mass, and ρ_{0d} is the *effective* location of unbalance mass. The *effective* unbalance eccentricity is defined as the multiplication of *effective* mass (m_e) and *effective* location of unbalance mass (ρ_{0d}), with the units kg-m. This rotating force excites the dynamics of the assembly, resulting in deflections—i.e., the dynamic components of radial throw—along the x and y directions. The resulting dynamic portion of the radial throw, ρ_d, can be given as

$$\boldsymbol{\rho_d} e^{j\omega t} = \begin{Bmatrix} \rho_{dx} \\ \rho_{dy} \end{Bmatrix} e^{j\omega t} = m_e \rho_{0d}\omega^2 [H(j\omega)]_\Omega \begin{Bmatrix} 1 \\ -j \end{Bmatrix} e^{j\omega t}, \tag{4}$$

where $[H(j\omega)]_\Omega$ is the spindle-speed dependent frequency response functions (FRFs) of the spindle in the form of receptance (displacement/force). This formulation assumes that the FRFs are obtained at different operational speeds (Ω) and thus capture the rotational effects on dynamics. The radial throw can now be written as

$$\boldsymbol{\rho} e^{j\omega t} = \begin{Bmatrix} \rho_x \\ \rho_y \end{Bmatrix} e^{j\omega t} = (\boldsymbol{\rho_0} + \boldsymbol{\rho_d}) e^{j\omega t}, \tag{5}$$

where $\boldsymbol{\rho_0}$ is the quasi-static radial throw measured at the "zero" speed. This zero-speed radial throw only arises from the kinematic motion of the geometric center (rather than the mass center), and during rotations, it can be expressed as

$$\boldsymbol{\rho_0} e^{j\omega t} = \begin{Bmatrix} \rho_{0x} e^{j\phi_{0x}} \\ \rho_{0y} e^{j\phi_{0y}} \end{Bmatrix} e^{j\omega t} \tag{6}$$

where ϕ_{0x} and ϕ_{0y} are the orientations of the x and y components of quasi-static radial throw. Eqs. (4), (5) and (6) can be combined and written as

$$\begin{Bmatrix} \rho_x \\ \rho_y \end{Bmatrix} = \begin{Bmatrix} \rho_{0x} e^{j\phi_{0x}} \\ \rho_{0y} e^{j\phi_{0y}} \end{Bmatrix} + m_e \rho_{0d}\omega^2 \{H(j\omega)\}_\Omega \begin{Bmatrix} 1 \\ -j \end{Bmatrix}, \tag{7}$$

This expression considers that, in general, the quasi-static radial throw follows an elliptical (with circle being a specific case) trajectory, with values $\rho_{0x}e^{j\phi_{0x}}$ and $\rho_{0y}e^{j\phi_{0y}}$ in the x and y directions, respectively. The presented model assumes that (1) the microtool is rigid, that is, the contributions of modes of the microtool on the tool-tip radial throw are negligible as compared to those originating from the interaction of the quasi-static radial throw and dynamics of the spindle; and (2) the geometric errors of the microtool are negligible.

3. Experimental methods

The experimental setup used for characterizing the dynamics is shown in Fig. 3. A repeatable impact excitation system (IES) is used to provide impact excitations to the spindle [33]. The IES consists of an electromagnet, a flexure to provide one dimensional motion to the attached impact hammer and electronics for precise actuation. The electromagnet used in the IES attracts a flexure-based assembly (which holds the impact hammer (PCB 086E80)) to provide an initial deflection. Once released, the flexure assembly hits the structure to provide high bandwidth impulsive excitations [21]. The IES can be used to provide excitations in x and y directions by changing its orientation. Fig. 3 shows the IES providing excitations in y direction.

Two laser Doppler vibrometers (LDVs) are used to measure the radial motions of the attached microtool. The LDVs are mounted on a 6-axis precision mount (Thorlabs, K6X) to facilitate precise adjustments of the laser position and orientation. The two lasers are aligned in a mutually-perpendicular fashion following the approach mentioned in [21]. The x and y axes, as shown in Fig. 1, are dictated by the direction of the two lasers. A displacement decoder (DD-500 analog displacement decoder) is used for the LDV systems (Polytec OFV-552), providing a frequency bandwidth of 1.5 MHz and picometer-level resolution.

The data is acquired using a data acquisition system (NI PXI-1033 chassis with a PXI-6115 board). The channels are synchronized to avoid any phase errors in the measurements. To provide automated and repeatable impact excitations, an output voltage signal from the NI system is amplified and sent to the electromagnet to achieve precise and repeatable release of the IES system. The LabVIEW code is used to collect the data from the NI system at a user-defined sampling rate. In this work, a sampling rate of 1 MHz is used. The data is then processed using a frequency domain filtering approach in MATLAB as presented in [21].

Radial throw in the x and y directions is obtained using the steps described in [10]. The displacement data is high-pass filtered with a cut-off frequency of 10 Hz to remove the low frequency drift. After averaging 500 revolutions, a sinusoidal function is fitted to the cycle-by-cycle averaged data in the least-squares sense to calculate the magnitude (ρ_x, ρ_y) and phase (ϕ_x, ϕ_y) associated with the fundamental component in radial x and y directions at the rotational speed of the spindle (See Fig. 4).
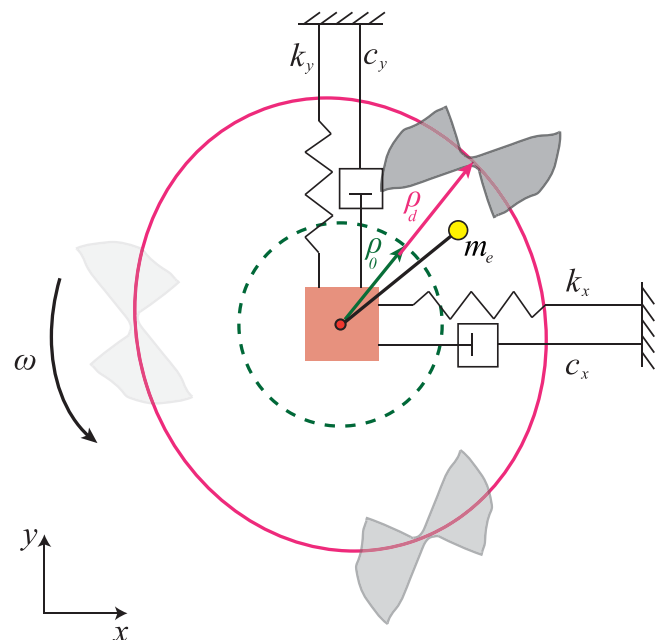

Fig. 2. A schematic diagram to explain the mathematical formulation relating the effect of unbalance eccentricity on radial throw.
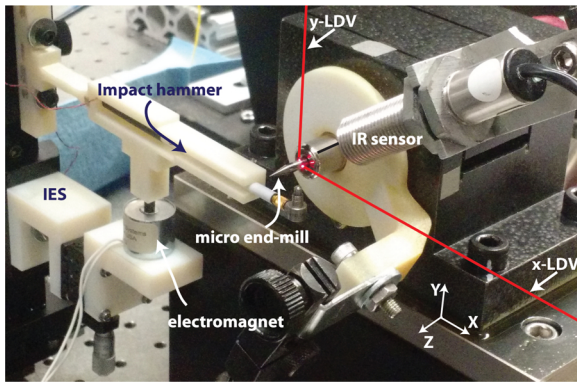
Fig. 3. The experimental setup used for dynamic characterization of spindle using the IES.
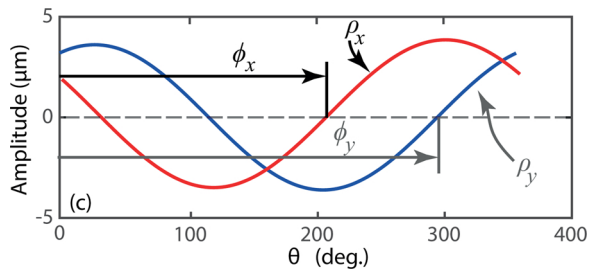

Fig. 4. Radial throw components at the fundamental (one-per-rev) frequency extracted to obtain the magnitude and phase of the fundamental displacement components in x and y directions.

4. Model application

To apply this formulation to our case, two sets of information are needed: the speed-dependent FRFs $[H(j\omega)]_\Omega$, and the model parameters $m_e\rho_{0d}$, ρ_{0x}, ρ_{0y}, ϕ_{0x} and ϕ_{0y}. As shown in our previous work [21,34], the dynamic response of UHS spindles changes with spindle speed.

To obtain the speed-dependent frequency response functions, we followed the spindle-dynamics characterization approach presented in [21]. The microtool used for the radial throw measurements was attached to the spindle. The spindle was then rotated at the desired speed, and the dynamic excitations to the system was provided using the IES [33] at the microtool shank at 2 mm away from the spindle nose ($z = 2$ mm) in the x and y directions using the IES. The ensuing dynamic response along the x and y directions was measured from the tool shank (at $z = 2$ mm) using the LDVs. This procedure was repeated for the five spindle speeds (60, 80, 100, 120, 130 krpm), and for each speed, the data was post-processed to obtain a 2×2 FRF matrix,

$$[H(j\omega)]_\Omega = \begin{bmatrix} H_{xx}(j\omega) & H_{xy}(j\omega) \\ H_{yx}(j\omega) & H_{yy}(j\omega) \end{bmatrix},$$

$$(8)$$

which includes both direct and cross components.

The magnitude plots of the obtained speed-dependent FRFs are given in Fig. 5. Although the rotational effects are most prominent in the vicinity of resonance frequencies (e.g., inducing mode splitting), the changes in spindle speed also cause relatively significant changes to the FRF magnitudes at frequencies relevant to this work (see the insets). Since the radial throw measurements in this work focus on the one-per-rev component, the relevant frequencies are those that correspond to spindle speeds used during the measurements, e.g., 1 kHz for 60 krpm.

The proposed method can be used to calibrate the model parameters ($m_e\rho_{0d}$, ρ_{0x}, ρ_{0y}, ϕ_{0x} and ϕ_{0y}) using the speed-dependent dynamics of the
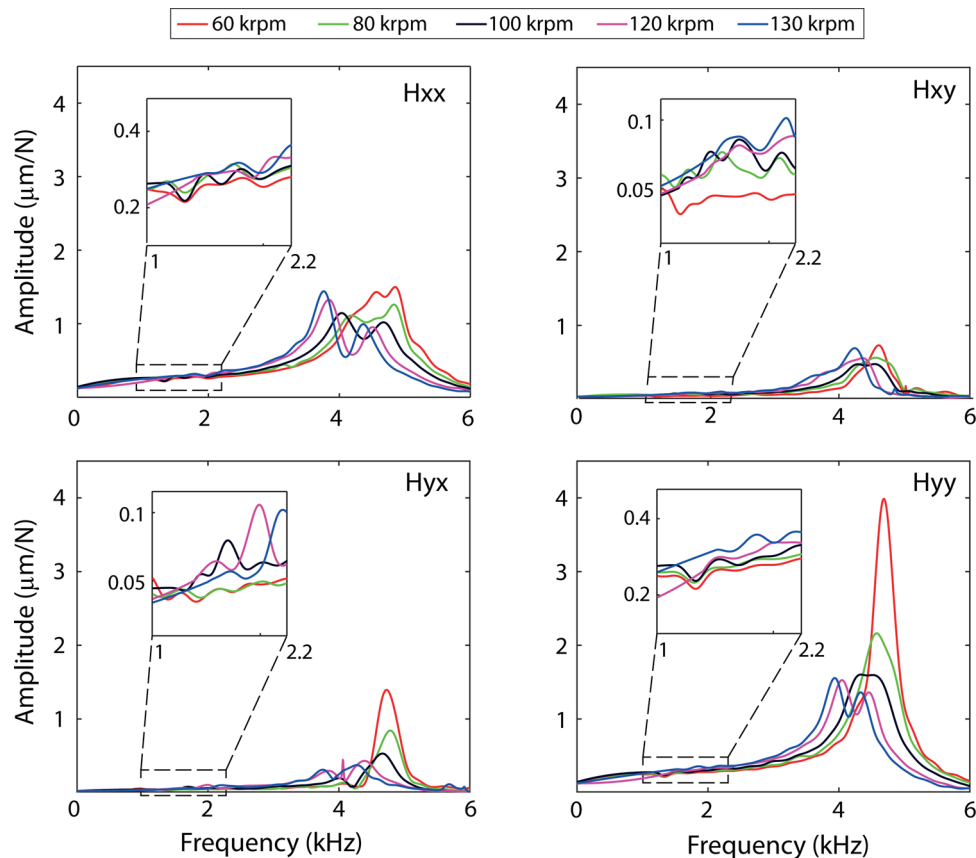

Fig. 5. Magnitude of $[H(j\omega)]_\Omega$ at different spindle speeds obtained from dynamic testing at an axial location of 2 mm. For references to the colors used in, readers are referred to the web version of this paper.

Table 1
A comparison between the measured and the predicted radial throw at 2 mm.

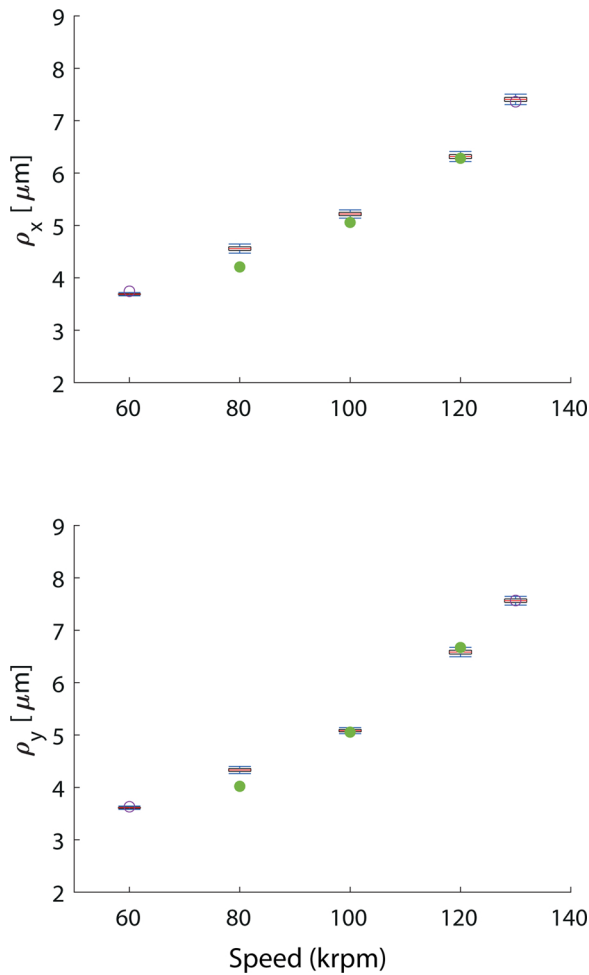| Speed	Radial throw, x			Radial throw, y			Phase difference, y-x	
(rpm)	Measured (μm)	Predicted (μm)	Error (%)	Measured (μm)	Predicted (μm)	Error (%)	Measured (°)	Predicted (°)
60 k	3.69 ± 0.01	3.73	1.13	3.61 ± 0.01	3.61	0.01	−88.89	−87.96
80 k	4.56 ± 0.03	4.20	7.89	4.33 ± 0.03	4.01	7.47	−90.33	−89.01
100 k	5.22 ± 0.03	5.05	3.17	5.08 ± 0.02	5.05	0.66	−90.19	−89.87
120 k	6.31 ± 0.04	6.29	0.42	6.58 ± 0.04	6.67	1.38	−89.09	−88.53
130 k	7.41 ± 0.04	7.37	0.50	7.56 ± 0.03	7.58	0.19	−90.28	−90.67

Fig. 6. Comparison of radial throw in x and y directions at an axial location of 2 mm. The speeds used to obtain model parameters are depicted by hollow circles (60 krpm and 130 krpm). The predictions at other speeds are depicted by filled circles.

Fig. 7. Comparison of radial throw in x and y directions at an axial location of 15 mm. The speeds used to obtain model parameters are depicted by hollow circles (60 krpm and 130 krpm). The predictions at other speeds are depicted by filled circles.
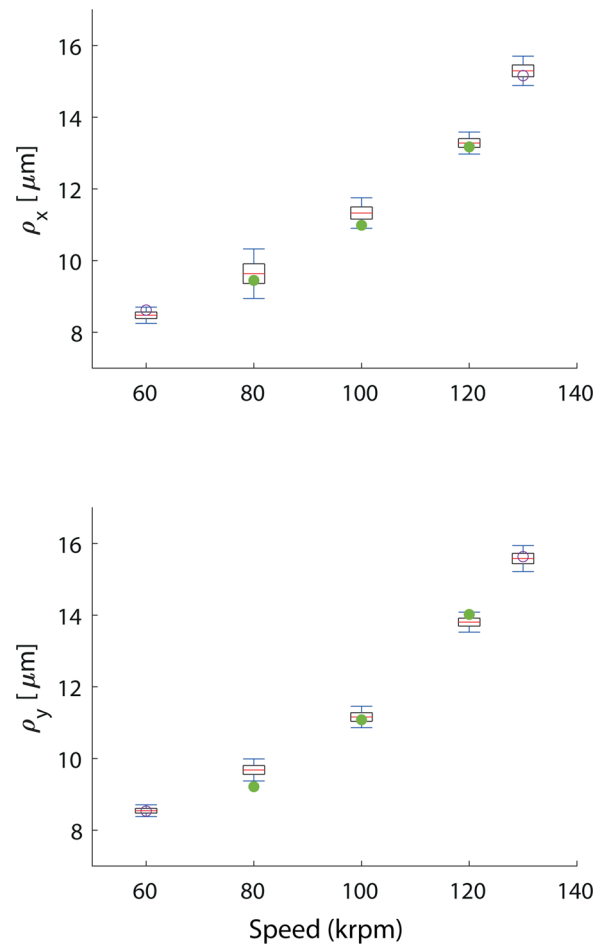
Table 2
A comparison between the calculated and the predicted radial throw at tool-tip (15 mm).

| Speed	Radial throw, x			Radial throw, y			Phase difference, y-x	
(rpm)	Calculated (μm)	Predicted (μm)	Error (%)	Calculated (μm)	Predicted (μm)	Error (%)	Calculated (°)	Predicted (°)
60 k	8.47 ± 0.09	8.62	1.70	8.54 ± 0.07	8.53	0.13	−89.69	−88.57
80 k	9.63 ± 0.28	9.45	1.95	9.68 ± 0.12	9.21	4.83	−90.89	−89.22
100 k	11.33 ± 0.17	10.99	3.01	11.16 ± 0.12	11.08	0.69	−89.70	−90.15
120 k	13.28 ± 0.12	13.17	0.80	13.81 ± 0.11	14.02	1.55	−89.84	−89.24
130 k	15.30 ± 0.16	15.16	0.87	15.58 ± 0.14	15.63	0.34	−90.40	−90.90
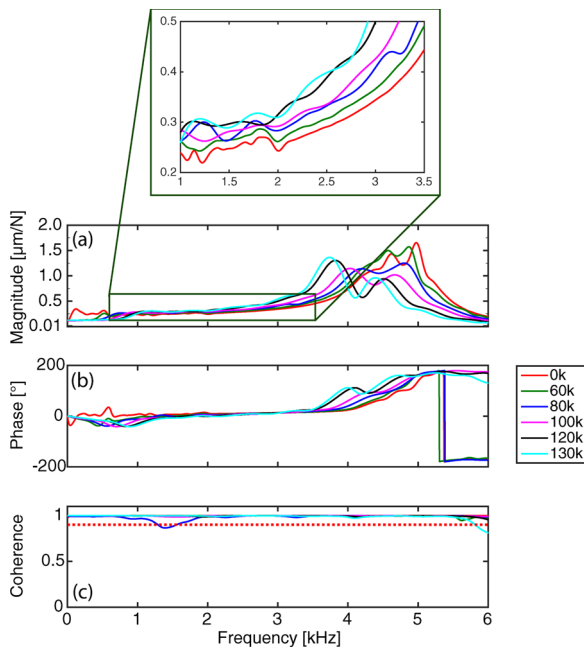
Fig. 8. Frequency response functions of the UHS spindle in x direction at different spindle speeds obtained from dynamic testing: (a) Magnitude of $[H_{xx}(j\omega)]_\Omega$ (b) Phase of $[H_{xx}(j\omega)]_\Omega$ (c) Coherence of $[H_{xx}(j\omega)]_\Omega$ obtained using 15 repetitions.
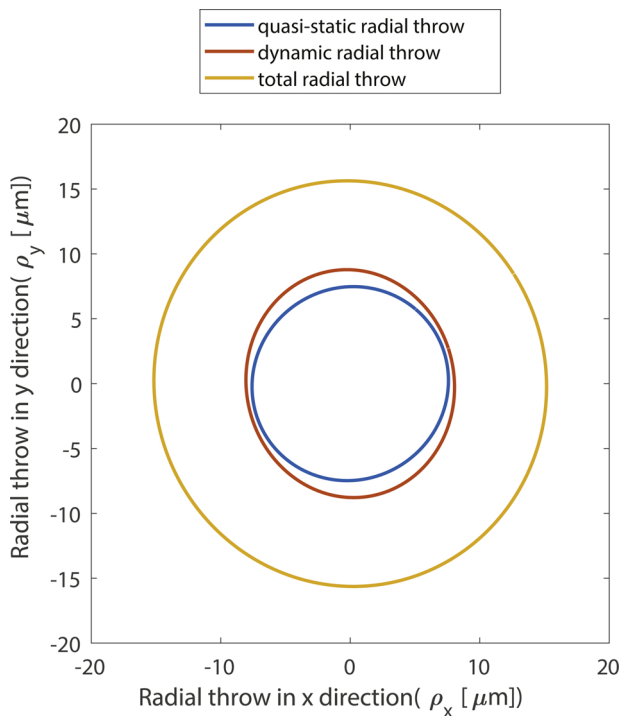

Fig. 9. Orbit plot of radial throw showing the static and dynamic components of radial throw at 130 krpm at the axial location of 15 mm, i.e., tool-tip.

spindles and speed dependent radial throw information. As seen in Eq. (7), there are five unknown parameters, necessitating the use of a minimum of five equations. The radial throw at two different different speeds in two different directions (x and y) give a total of four equations in the complex domain. Corresponding to these four equations, the data from the two spindle speeds provide eight values (real and imaginary parts from each of the x and y components.) These equations are then used to obtain the five parameters using a least square curve-fitting

approach.

In the current work, two different cases are shown. First, the dynamics measured at the axial location of 2 mm is used to predict the radial throw at the axial location of 2 mm. Second, the dynamics measured at the axial location of 2 mm is used to predict the radial throw at the axial location of 15 mm. In each of the cases, radial throw at two speeds is used for calibration and the remaining speeds are used for validation.

The calibrated model parameters obtained at the axial location of 15 mm are shown below. These parameters are obtained using the radial throw at 60 krpm and 130 krpm.

$$m_e\rho_{0d} = 1.20 \times 10^{-7}\text{kg. m}, \quad \rho_{0x} = 7.58\,\mu\text{m},$$
$$\rho_{0y} = 7.48\,\mu\text{m}, \quad \phi_{0x} = 48.35\,\text{deg.}, \quad \phi_{0y} = -39.81\,\text{deg.}$$

As expected, the quasi-static radial throw magnitudes in x and y directions are very close to each other, and the difference between the x and y phase angles is very close to 90°. This indicates that the quasi-static trajectory closely resembles a circle (also see Fig. 9).

Table 1 provides measured and predicted speed-varying radial throw and the error percentage considering the mean value of the measured parameter as a reference at 2 mm axial location. An average error of 3.8% and 3.2% is observed in the x and y directions, respectively. Fig. 6 presents the results of Table 1 in a graphical format, where the predicted values are close to the measured values, except at 80 krpm. Similarly, Table 2 shows the comparison of speed-varying radial throw at the tool tip (15 mm) between the calculated (using [10], briefly described in Section 2) and the predicted values. In this case, we observe a lower average percentage error of 1.9% and 2.4% in the x and y directions, respectively. Again, the prediction at 80 krpm shows a significantly larger error. At other speeds, the predicted radial throw magnitudes are within the $\pm 2.5\bar{\sigma}$ bounds (refer to Fig. 7).

To further explore the 80 krpm case, coherence was checked for all speeds. As shown in Fig. 8(c), 80 krpm case shows a slight drop in the coherence value near the frequency of interest. The synchronous component of 80 krpm (1.33 kHz) has a coherence value of 0.88, which suggests that the quality of dynamic data at 80 krpm may be the source of error. Fig. 9 shows the quasi-static and dynamic components of radial throw in the x and y directions at 130 krpm in the form of orbit plots. It is observed that the quasi-static component closely resembles a circle. This is expected since the quasi-static magnitudes in the x and y directions are close. The dynamic component is higher in the y direction (major-axis of ellipse closer to y-axis, compared to x-axis) which is why the total radial throw is larger in y as shown in Table 2. Overall, it is concluded that the presented simplified model can be utilized to capture the effect of spindle speed on radial throw resulting from the dynamic response due to rotating unbalance. It is also observed that the dynamic data at an axial location of 2 mm is successful in predicting the radial throw at 15 mm. Hence, in this particular case, dynamic tilt effects are not significant.

5. Summary and conclusions

In this work, a simplified model to capture the effect of tool-collet-spindle assembly dynamics on radial throw was proposed. The model consists of a quasi-static and a dynamic component in the x and y directions. The dynamic component of radial throw is obtained as a response to rotating unbalance excitation. To calibrate the model parameters, speed-dependent FRFs of the spindle were obtained, and the radial throw measurements from two speeds were used. The average error between the predictions and measurements were seen to be less than 2.4% at the tool tip. As such, this simplified model can be used to predict the dynamics driven changes in radial throw at different spindle speeds.

The current model has two limitations: (1) it assumes that changes in the dynamic component of the radial throw with tilt (i.e., angular

frequency response functions) are not significant with changing speed. If this assumption is violated, then a more detailed modeling approach will be needed to account for the tilt motions; (2) the current modeling approach assumes that the tool-dominant modes are significantly far from the spindle operating speeds, such that their impact is negligible. This may become important to consider for much higher speeds (∼ 500 krpm).

Conflicts of interest

The authors declare that they have no known competing financial interests or personal relationships that could have appeared to influence the work reported in this paper.

Acknowledgements

References

[1] Wilson ME, Kota N, Kim YT, Wang Y, Stolz DB, LeDuc PR, et al. Fabrication of circular microfluidic channels by combining mechanical micromilling and soft lithography. Lab Chip 2011;11(8):1550.

[2] Dornfeld D, Min S, Takeuchi Y. Recent advances in mechanical micromachining. CIRP Ann – Manuf Technol 2006;55(2):745–68.

[3] Camara MA, Campos Rubio JC, Abrão AM, Davim JP. State of the art on micro-milling of materials, a review. J Mater Sci Technol 2012;28(8):673–85.

[4] Filiz S, Conley CM, Wasserman MB, Burak Ozdoganlar O. An experimental investigation of micro-machinability of copper 101 using tungsten carbide micro-endmills. Int J Mach Tools Manuf 2007;47(7–8):1088–100.

[5] Korkmaz E, Onler R, Burak Ozdoganlar O. Micromilling of poly(methyl methacrylate, PMMA) using single-crystal diamond tools. Proc Manuf 2017;10:683–93.

[6] Yu JZ, Korkmaz E, Berg MI, LeDuc PR, Burak Ozdoganlar O. Biomimetic scaffolds with three-dimensional undulated microtopographies. Biomaterials 2017;128:109–20.

[7] Bediz B, Korkmaz E, Khilwani R, Donahue C, Erdos G, Falo LD, et al. Dissolvable microneedle arrays for intradermal delivery of biologics: fabrication and application. Pharm Res 2014;31(1):117–35.

[8] Lee K, Ahn SH, Dornfeld DA, Wright PK. The effect of run-out on design for manufacturing in micro-machining process. Proceedings of the ASME international mechanical engineering congress and exposition. 2001. p. 11–7.

[9] Lee K, Dornfeld DA. A study of surface roughness in the micro-end-milling process. Laboratory for Manufacturing and Sustainability; 2004.

[10] Nahata S, Onler R, Shekhar S, Korkmaz E, Burak Ozdoganlar O. Radial throw in micromachining: measurement and analysis. Precis Eng 2018;54:21–32.

[11] Nahata S, Onler R, Burak Ozdoganlar O. Radial throw in micromilling: a simulation-based study to analyze the effects on surface quality and uncut chip thickness. J Micro Nano-Manuf 2019;7(1):10907.

[12] Kline WA, DeVor RE. The effect of runout on cutting geometry and forces in end milling. Int J Mach Tool Des Res 1983;23(January (2–3)):123–40.

[13] Li XP, Li HZ. Theoretical modelling of cutting forces in helical end milling with cutter runout. Int J Mech Sci 2004;46(September (9)):1399–414.

[14] Afazov SM, Ratchev SM, Segal J. Modelling and simulation of micro-milling cutting forces. J Mater Process Technol 2010;210(November (15)):2154–62.

[15] Afazov SM, Ratchev SM, Segal J, Popov AA. Chatter modelling in micro-milling by considering process nonlinearities. Int J Mach Tools Manuf 2012;56(May):28–38.

[16] Zhang X, Ehmann KF, Yu T, Wang W. Cutting forces in micro-end-milling processes. Int J Mach Tools Manuf 2016;107(August):21–40.

[17] Kundan K, Kartik SV, Singh R. Stability modeling with dynamic run-out in high speed micromilling of Ti6Al4V. Int J Mech Sci 2019;150(January):677–90.

[18] ISO. ISO 230-7 (2015): test code for machine tools – geometric accuracy of axes of rotation. 2015.

[19] Nahata S, Onler R, Korkmaz E, Burak Ozdoganlar O. Radial throw at the cutting edges of micro-tools when using ultra-high-speed micromachining spindles. Procedia manufacturing 26. Elsevier; 2018. p. 1517–26. January.

[20] Lu X, Jamalian A, Graetz R. A new method for characterizing axis of rotation radial error motion: part 2. Experimental results. Precis Eng 2011;35(1):95–107.

[21] Bediz B, Arda Gozen B, Korkmaz E, Burak Ozdoganlar O. Dynamics of ultra-high-speed (UHS) spindles used for micromachining. Int J Mach Tools Manuf 2014;87:27–38.

[22] Bediz B, Burak Ozdoganlar O. Rotational dynamics of micro-scale cutting tools. Precis Eng 2019;60(November):1–11.

[23] Liu X, Jun MBG, DeVor RE, Kapoor SG. Cutting mechanisms and their influence on dynamic forces, vibrations and stability in micro-endmilling. ASME 2004 international mechanical engineering congress and exposition. 2004. p. 583–92.

[24] Hekman KA, Liang SY. In-process monitoring of end milling cutter runout. Mechatronics 1997;7(1):1–10.

[25] Bao WY, Tansel IN. Modeling micro-end-milling operations. Part II: Tool run-out. Int J Mach Tools Manuf 2000;40(15):2175–92.

[26] Nakkiew W, Lin CW, Tu JF. A new method to quantify radial error of a motorized end-milling cutter/spindle system at very high speed rotations. Int J Mach Tools Manuf 2006;46(7–8):877–89.

[27] Jun MB, DeVor RE, Kapoor SG. Investigation of the dynamics of microend milling-part II: Model validation and interpretation. J Manuf Sci Eng 2006;128(4):901–12.

[28] Malekian M, Park SS, Jun MBG. Modeling of dynamic micro-milling cutting forces. Int J Mach Tools Manuf 2009;49(7–8):586–98.

[29] Anandan P, Abhinandan K, Tulsian S, Donmez A, Burak Ozdoganlar O. A Technique for measuring radial error motions of ultra-high-speed miniature spindles used for micromachining. Precis Eng 2012;36(1):104–20.

[30] Prashanth Anandan K, Burak Ozdoganlar O. Analysis of error motions of ultra-high-speed (UHS) micromachining spindles. Int J Mach Tools Manuf 2013;70(July):1–14.

[31] Sinha JK, Lees AW, Friswell MI. Estimating the static load on the fluid bearings of a flexible machine from run-down data. Mech Syst Signal Process 2004;18(6):1349–68.

[32] Knapp B, Arneson D. Dynamic characterization of a micro-machining spindle. International conference on micromanufacturing (ICOMM), No. 108 2014.

[33] Bediz B, Korkmaz E, Burak Ozdoganlar O. An impact excitation system for repeatable, high-bandwidth modal testing of miniature structures. J Sound Vib 2014(13):2743–61.

[34] Bediz B, Romero LA, Burak Ozdoganlar O. Three dimensional dynamics of rotating structures under mixed boundary conditions. J Sound Vib 2015;358(December):176–91.